The Journal of Chemical Physics

RESEARCH ARTICLE | NOVEMBER 11 2024

Energy relaxation of N_2O in gaseous, supercritical, and liquid xenon and SF_6

Kai Töpfer ; Shyamsunder Erramilli ; Lawrence D. Ziegler ; Markus Meuwly

J. Chem. Phys. 161, 184503 (2024)
https://doi.org/10.1063/5.0235760

AIP Publishing

The Journal
of Chemical Physics

ARTICLE

pubs.aip.org/aip/jcp

Energy relaxation of N_2O in gaseous, supercritical, and liquid xenon and SF_6

Cite as: J. Chem. Phys. 161, 184503 (2024); doi: 10.1063/5.0235760
Submitted: 29 August 2024 • Accepted: 4 October 2024 •
Published Online: 11 November 2024

Kai Töpfer,[1] **Shyamsunder Erramilli,**[2] **Lawrence D. Ziegler,**[3] **and Markus Meuwly**[1,4,a)]

AFFILIATIONS

[1] Department of Chemistry, University of Basel, Klingelbergstrasse 80, CH-4056 Basel, Switzerland
[2] Department of Physics and the Photonics Center, Boston University, 590 Commonwealth Ave., Boston Massachusetts 02215, USA
[3] Department of Chemistry and the Photonics Center, Boston University, 8 St. Mary's St., Boston Massachusetts 02215, USA
[4] Department of Chemistry, Brown University, Providence, Rhode Island 02912, USA

[a)] **Author to whom correspondence should be addressed:** m.meuwly@unibas.ch

ABSTRACT

Rotational and vibrational energy relaxation (RER and VER) of N_2O embedded in xenon and SF_6 environments ranging from the gas phase to the liquid, including the supercritical regime, is studied at a molecular level. Calibrated intermolecular interactions from high-level electronic structure calculations, validated against experiments for the pure solvents, were used to carry out classical molecular dynamics simulations corresponding to experimental state points for near-critical isotherms. The computed RER rates in low-density solvents of $k_{\mathrm{rot}}^{\mathrm{Xe}} = (3.67 \pm 0.25) \times 10^{10}\ \mathrm{s}^{-1}\ \mathrm{M}^{-1}$ and $k_{\mathrm{rot}}^{\mathrm{SF_6}} = (1.25 \pm 0.12) \times 10^{11}\ \mathrm{s}^{-1}\ \mathrm{M}^{-1}$ compare well with the rates determined by the analysis of two-dimensional infrared experiments. Simulations find that an isolated binary collision description is successful up to solvent concentrations of ~4 M. For higher densities, including the supercritical regime, the simulations do not correctly describe RER, probably due to the neglect of solvent–solute coupling in the analysis of the rotational motion. For VER, the near-quantitative agreement between simulations and pump–probe experiments captures the solvent density-dependent trends.

INTRODUCTION

Understanding the precise molecular level details of rotational and vibrational energy relaxation dynamics in high density gas and supercritical fluid (SCF) solutions is of fundamental importance for the description, optimization, and control of chemical reactivity in inherently dense media. For example, dense fluids at high temperatures and pressures, often in supercritical (sc) regimes, are solvent environments where many combustion reactions occur.[1–3] Furthermore, SCFs offer the possibility for selective control of chemical processes including energy relaxation/transfer dynamics and have already been successfully employed in a range of applications.[4–10] Aside from offering the "green" potential to replace organic solvents (e.g., scH_2O or scCO_2), local density augmentation and the dynamics associated with the long-spatial correlations that develop in near critical state points contribute to the special solvation properties of near critical fluids.[4,11,12] These density correlation length increases result in a corresponding correlation relaxation time increase at the critical point, often described as critical slowing and evident in scattering experiments[13–15] and simulations.[16,17]

In prior ultrafast studies of dense gas and supercritical fluid solutions, two-dimensional infrared (2DIR) experiments have revealed rates of rotational energy relaxation (RER) as a function of solvent density for the N_2O asymmetric stretching mode (ν_{as}) in SF_6 and Xe even in the absence of any rotational features in the corresponding ν_{as} rovibrational spectrum.[18–20] Pump–probe measurements provide vibrational energy relaxation (VER) rates for these same high density state points. A simple isolated binary collision (IBC) model was sufficient to describe the RER of N_2O ν_{as} up to SF_6 and Xe solvent densities of ≈4M for $T \leq 1.01 T_c$ isotherms derived from 2DIR measurements.[20] However, the RER dynamics of N_2O in these two similar non-dipolar solvents show different concentration dependencies as the critical density is approached and where many-body effects begin to play a larger role for solvation.[20] The RER of N_2O is slower than the IBC predicted rates in the density region (≈4M–≈6M) of the SF_6 critical point [$\rho_c(SF_6) = 5.09$M] and attributed to the longer length scale, slower density fluctuations coupling to the closest N_2O solvation shells. However, no such slowing effect was observed for N_2O RER in xenon. For xenon densities $> \sim 4$M, the RER rate monotonically increased through the critical point region [$\rho_c(\text{Xe}) = 8.40$M]. It was hypothesized that the many-body interactions at the higher critical density for the xenon solvent shielded the N_2O rotors from coupling to the long correlation length fluctuations. N_2O rotational relaxation in both solvents is a highly efficient process. Following ν_{as}, excitation rotational equilibrium is re-established after 1.7 and 2.4 collisions in SF_6 and Xe, respectively, in the IBC density region.[20]

Rotational and vibrational equilibria are established on very different time scales following N_2O ν_{as} excitation in these high density gas and SCF SF_6 and Xe solvents.[20] While only a couple of collisions are required for N_2O rotations to thermalize in both solvents, the VER of N_2O may take hundreds of collisions or more to return the molecule fully to thermal equilibrium. The density dependence of N_2O VER is also strikingly different in xenon and SF6, and underscores that VER has a highly variable rate due to the inherently quantum nature ($\hbar\omega_{\text{vib}} = kT$) of this relaxation mechanism. The N_2O ν_{as} lifetime is ≈300 times shorter in SF_6 than in xenon because xenon has no possible resonant V → V, solute → solvent, energy transfer relaxation pathway as found for relatively efficient VER from N_2O ν_{as} in SF_6. The first step in N_2O ν_{as} VER in SF_6 is the collision enabled intramolecular relaxation to the N_2O symmetric stretching mode before a much slower return to the ground vibrational state. Furthermore, VER is nearly an order of magnitude slower for this initial VER component in SF_6 as compared to RER, and a critical slowing effect is not as clearly evident.[20] The density dependence of the N_2O ν_{as} rovibrational absorption line shapes in SF_6 and xenon was well-captured in a previous classical MD simulation study.[21] Even the rovibrational spectral contours, inherently determined by J, M quantum transition selection rules, were accurately duplicated by these classical simulation results. The goal of this article is to test the ability of this same simulation approach to capture the previously reported N_2O ν_{as} rotational and vibrational relaxation dynamics determined by these 2DIR and pump–probe measurements spanning the dense gas to the supercritical density regime in SF_6 and Xe.

Relaxation phenomena in liquids provide valuable information about intermolecular interactions and coupling between solvent and solute modes. In the present work, the RER and VER of N_2O as the solute immersed in Xe and SF_6 as atomic and molecular solvents at a wide range of densities are investigated from atomistic simulations. The environments are under conditions that range from gaseous to supercritical and regular liquids.

The present work is structured as follows: First, the methods are presented, followed by the validation of the intermolecular interactions. Next, results on the RER and VER of N_2O are presented and discussed. Finally, conclusions are drawn.

METHODS

Inter- and intramolecular interactions

The N_2O PES

The intramolecular potential energy surface (PES) of N_2O in its electronic ground state ($^1A'$) is provided by a machine-learned representation using the reproducing kernel Hilbert space (RKHS) method.[22,23] Reference energies at the CCSD(T)-F12/aug-cc-pVQZ level of theory were determined on a grid of Jacobi coordinates (R, r, θ) with r being the N–N separation, R being the distance between the center of mass of the diatom and the oxygen atom, and θ being the angle between the two distance vectors. All calculations were carried out using the MOLPRO package.[24] The full-dimensional RKHS model for a N_2O potential energy surface was originally developed for the investigation of N + NO collision reaction dynamics.[23] The Pearson coefficient R^2 of the RKHS representation and the full set of reference values is 0.999 83, and the root mean squared error (RMSE) between RKHS and reference energies up to 20 kcal/mol above the equilibrium structure (78 reference energies) is 0.13 kcal/mol.

The solvent PES

Intra- and intermolecular force field parameters for SF_6 were those from the work of Samios *et al.*[25] Intermolecular interactions were based on Lennard-Jones potentials only, and the parameters were optimized such that MD simulations of pure SF_6 reproduce the experimentally observed pVT state points for liquid and gas SF_6, as well as the states of liquid–vapor coexistence below and supercritical fluid above the critical temperature $T_c(SF_6) = 318.76$ K, respectively.[26,27] For Xe, the Lennard-Jones parameters were optimized to reproduce the pVT state points of gaseous, supercritical, and liquid Xe at different densities and temperatures below and above the critical temperature of $T_c(\text{Xe}) = 289.74$ K.[26,27]

The Xe–Xe Lennard-Jones (LJ) potential parameters for the van der Waals (vdW) potential energy contribution were fit to match experimental pVT state points of xenon, which were computed with a similar setup as used by Samios *et al.* to fit the force field parameters for SF_6.[25] A set of $N_{pVT} = 44$ experimentally measured pVT state points of xenon at temperatures (number of state points) 273.15 (5), 286.65 (3), 298.15 (12), 323.15 (12), and 373.15 K (12) was selected.[28] For each state point, a separate NVT molecular dynamics (MD) simulation was run using a Langevin thermostat with a friction coefficient of 0.1 ps^{-1}. The system contained 1200 Xe atoms; the structure was minimized, heated to the target temperature, and equilibrated for a total of 100 ps with a time step of 1 fs. Next, the average pressure was determined from a 300 ps simulation and compared with the experimental reference.[28] The xenon LJ parameters ϵ_{Xe} and $R_{\text{min,Xe}}$ were then optimized by the Nelder–Mead method[29] to minimize the relative root mean square error (rRMSE) between the sampled average and experimental pressures at respective volume and temperature,

$$\text{rRMSE} = \sqrt{\frac{1}{N_{pVT}} \sum_i^{N_{\text{PVT}}} \left(\frac{p_{\text{sim.},i}(V,T) - p_{\text{ref.},i}(V,T)}{p_{\text{ref.},i}(V,T)} \right)^2}. \quad (1)$$

The LJ parameter set with the lowest rRMSE was chosen after the rRMSE arguably reached a convergence limit for several tens of optimization steps.

Electrostatic solvent–solute interactions were computed based on a minimally distributed charge model (MDCM) for N_2O that correctly describes higher-order multipole moments.[30–32] For parameterization, a reference electrostatic potential (ESP) of N_2O in its linear equilibrium conformation was computed at the CCSD/aug-cc-pVTZ level using the Gaussian program package.[33] The optimized MDCM fit reproduces the ESP with a RMSE of 0.31 kcal/mol. For SF_6 in its octahedral equilibrium conformation, the ESP was computed at the MP2/aug-cc-pVTZ level of theory using the Gaussian program. The RMSE between the fitted ESP from MDCM and the reference ESP was 0.11 kcal/mol. Recently,[32] non-iterative polarization has also been included in MDCM, and this is also used here for N_2O, SF_6, and Xe. The polarizability of linear N_2O at the CCSD/aug-cc-pVTZ level is 2.85 Å^3 (with each atom contributing ~0.95 Å^3 per atom), compared with 2.998 Å^3 from experiment.[34] For Xe at the CCSD/aug-cc-pVTZ level, the computed value of 2.96 Å^3 compares with 4.005 Å^3 from experiment,[34] and for SF_6, the experimentally measured polarizability of 4.49 Å^3 was used and evenly distributed over the fluorine atoms (0.74 Å^3 per fluorine atom).[35]

The LJ parameters for N_2O ($\epsilon_\alpha, R_{\min,\alpha}$ with $\alpha = \{\mathrm{N}, \mathrm{O}\}$) were individually optimized for each N_2O atom by least-squares fitting using the trust region reflective algorithm[36] to best reproduce the N_2O–Xe and N_2O–SF_6 interaction energies, respectively. Reference energies were computed for a single N_2O molecule immersed within differently dense Xe or SF_6 clusters to sample gaseous, supercritical, and liquid solvent environments. For this, 50 cluster conformations for each solvent state were extracted from earlier MD simulations of different solvent concentrations.[21] The clusters contained 3, 7, and 10 xenon atoms and 2, 6, and 10 SF_6 molecules for gaseous, supercritical, and liquid samples within the radius of the first solvation shell around the N_2O center of mass of 6.5 and 7.5 Å, respectively. Cluster conformations were randomly extracted from the trajectories with the respective number of solvent atoms or molecules within the cluster radius maintained.

Counterpoise corrected reference interaction energies between N_2O and the solvent shell of the cluster were computed at the M06-2X/aug-cc-pVTZ level of theory including D3 dispersion corrections with the Gaussian program package.[33,37,38] Computations at the CCSD(T) level of theory, as done for the intramolecular N_2O potential, are not feasible for the interaction energies between N_2O and up to 10 Xe atoms or 10 SF_6 molecules.

Molecular dynamics simulations

Molecular dynamics simulations were performed with the CHARMM program package[39] including provisions for RKHS and MDCM.[22,30,32] Each system (N_2O in Xe and N_2O in SF_6 at given temperature and solvent concentration) was sampled from five independent MD simulations with initially random solute and solvent arrangements generated using the packmol code.[40] Each simulation was initially heated and equilibrated for 100 ps each, followed by 10 ns production simulations in the *NVT* ensemble using a time step $\Delta t = 1$ fs for the leapfrog integration scheme. In total, a total of 50 ns was sampled for each system condition.

The N_2O/Xe systems were simulated at a temperature of 291.2 K, and for N_2O/SF_6, the temperature was 321.9 K, of which both are slightly above the experimental critical temperatures for condensation of xenon and SF_6, respectively [$T_c(\mathrm{Xe}) = 289.74$ K, $T_c(SF_6) = 318.76$ K].[19,26,27] A Langevin thermostat (coupling 0.1 ps^{-1}) was used to maintain the temperature constant but was applied only to the solvent (Xe and SF_6) atoms. The positions and velocities of snapshots of the simulations were stored every 1 fs for analysis. As intermolecular vibrational energy transfer is slow,[20] the structure of N_2O was optimized and new velocities from a Boltzmann distribution at the simulation temperature were assigned to N_2O after the heating step. This ensures that the kinetic energies along the asymmetric, symmetric, and bending modes match the thermal energy with respect to the target simulation temperature.

The different simulation systems were prepared according to the conditions used in the experiments.[18–20] Table S1 summarizes the N_2O concentrations $c(N_2O)$, molar volumes V_m, and critical density ratios $\rho^* = \rho/\rho_c$ used in the simulations. The experimentally determined critical densities are $\rho_c = 1.11$ g/ml for xenon and $\rho_c = 0.74$ g/ml for SF_6, from which critical concentrations of 8.45 and 5.06 M for xenon and SF_6 are obtained, respectively.[26,27] In all setups, the simulation box contained one N_2O molecule and 600 Xe atoms or 343 SF_6 molecules, which corresponds to similar simulation box volumes for similar relative density ratios of the two solvents. In the original parameterization study, a simulation box containing 343 SF_6 molecules was used to fit temperature–pressure properties.[25]

In the MD simulations for N_2O in SF_6, electrostatic and polarization interactions were only computed between the N_2O solute and the SF_6 solvent. Electrostatic and polarization contributions to the SF_6 solvent–solvent interactions were neglected. Such a procedure ensures that the pure (liquid, gas) properties of the solvent are unaltered.

Analysis

Rotational relaxation

The RER times of the N_2O solute were determined by fitting single- or bi-exponential functions to the autocorrelation functions involving angular momentum-dependent quantities. The normalized correlation functions $C(t)$ for time-dependent scalar $(A(t))$,

$$C(t) = \frac{\langle A(0) \cdot A(t) \rangle}{\langle A(0)^2 \rangle}, \tag{2}$$

or vectorial ($\vec{A}(t) = \{A_x(t), A_y(t), A_z(t)\}$),

$$C(t) = \sqrt{\frac{1}{3} \sum_{i=x,y,z} \frac{\langle A_i(0) \cdot A_i(t) \rangle^2}{\langle A_i(0)^2 \rangle}}, \tag{3}$$

observables were computed for the time series of the rotational energy of N_2O, where $E_{\mathrm{rot}}(t) = |\vec{L}(t)|^2 / 2I(t)$, in which $I(t)$ is the moment of inertia, $|\vec{L}(t)|^2$ is the squared angular momentum, and $\vec{L}(t)$ is the angular momentum.

The amplitude A, RER rates $1/\tau_i$, and offset Δ of a single exponential function $C_1(t)$,

$$C_1(t) = A e^{-t/\tau} + \Delta, \tag{4}$$

were optimized to fit the sampled rotational energy correlation function from simulations. For the fit, the lower limit for the time was $t = 0.2$ ps, as had also been done for fitting the experimental results to avoid any pulse overlap effects,[20] and was restricted to $C(t) \geq 0$. It is noted that using a double exponential function does not provide improved representations of the data even near the critical point.

Vibrational relaxation

Transition rates $k_{i\to j} = \tau_{ij}^{-1}$ for the vibrational state transition $i \to j$ of the N_2O solute in solution were computed from a Landau–Teller model,[41–47]

$$k_{i\to j} = \frac{1}{\tau_{ij}(\omega_{ij})} = \gamma_{ij}\int_{-\infty}^{\infty} dt\, \exp(i\omega_{ij}t)\zeta(t), \tag{5}$$

with a proportionality factor γ_{ij} defined as

$$\gamma_{ij} = \frac{2\hbar^{-2}}{1 + \exp(-\beta\hbar\omega_{ij})} \cdot Q(\omega_{ij}), \tag{6}$$

$$Q(\omega_{ij}) = \frac{\beta\hbar\omega_{ij}}{2} \coth\left(\frac{\beta\hbar\omega_{ij}}{2}\right), \tag{7}$$

which includes $\beta = 1/(k_B T)$ and a quantum correction factor $Q(\omega)$ for the classically obtained correlation function $\zeta(t)$.[43,48] Here, $\zeta(t)$ is the time-dependent friction acting on the oscillation of the solute and is derived from the correlation function,

$$\zeta(t) = \langle V_{ij}(t) \cdot V_{ji}(0)\rangle, \tag{8}$$

of the classical solute–solvent interaction friction potential $V_{ij}(t)$. The solute–solvent interaction is obtained from the solute–solvent force $\vec{F}_{\mathrm{int}}(t)$ projected along the normal mode vector $\vec{q}_i$ by the sum over the solute atoms α according to

$$V_{ij}(t) = \mu_i \sum_{\alpha} \frac{1}{m_\alpha} \frac{\partial V_{\mathrm{int}}(t)}{\partial \vec{q}_{i,\alpha}(t)} \cdot \vec{q}_{i,\alpha}(t) = -\sum_{\alpha} \vec{F}_{\mathrm{int},\alpha}(t) \cdot \vec{q}_{i,\alpha}(t), \tag{9}$$

where m_α is the atom mass of α and μ_i is the reduced mass of normal mode i.[43] Because a quantum mechanical correlation function was replaced by its classical analog, quantum correction factors Q have been introduced.[46,48,49] The typical behavior of $Q(\omega)$ is ≈ 1 for $\hbar\omega \ll k_B T$ $[\lim_{\omega\to 0} Q(\omega) = 1]$, whereas $Q(\omega)$ can become significantly larger than 1 for $\hbar\omega \gtrsim k_B T$.

RESULTS

Validation of inter- and intramolecular interactions

For investigating the RER and VER of N_2O in gaseous, supercritical, or liquid Xe or SF_6 environments, an accurate representation of the solute–solvent interaction is crucial.[18–20] The results of the parameter optimization for the intermolecular interactions are summarized next.

Solute potential

To establish the quality of the N_2O PES, the vibrational modes were determined by solving the 3D nuclear Schrödinger equation using the DVR3D[50] package. The computed fundamental asymmetric, symmetric, and bending vibrations were at $\nu_{as} = 2229$ cm^{-1}, $\nu_s = 1291$ cm^{-1}, and $\nu_b = 598$ cm^{-1} and agree well with 2224, 1285, and 589 cm^{-1}, respectively, from experiments in the gas phase.[51–53] For the bending overtone ($2\nu_b$), the computations yield 1184 cm^{-1} compared with 1168 cm^{-1} from experiments.[51–53]

Solvent potential

The Xe and SF_6 solvent potential models [for Xe–Xe interaction see Fig. 1(a)] aim at accurately reproducing the experimentally measured pVT state points. The atomic LJ parameters for SF_6 were already fitted to match reference pVT state points of pure gaseous, supercritical, and liquid SF_6 systems.[25] In contrast, for xenon, the previously used LJ parameters were fitted to match dilute gas macroscopic properties such as virial coefficient, viscosity, and thermal conductivity over a wide temperature range but not specifically for correct phase transition and supercritical fluid properties.[54] As described above, the LJ parameters were refitted to reproduce the reference system pressure of pure xenon under 44 different density and temperature conditions.[28] Figure 1(a) shows the measured reference isotherms in the pVT diagram (dashed lines) and the computed pVT state points from simulations using the optimized LJ parameters with the lowest relative RMSE of 15.1% between reference and computed system pressures (absolute RMSE of 32.7 Pa). This is an improvement by a factor of ~5 (relative RMSE of 75.1%; absolute RMSE of 124.3 Pa) when using the original parameters.[54]

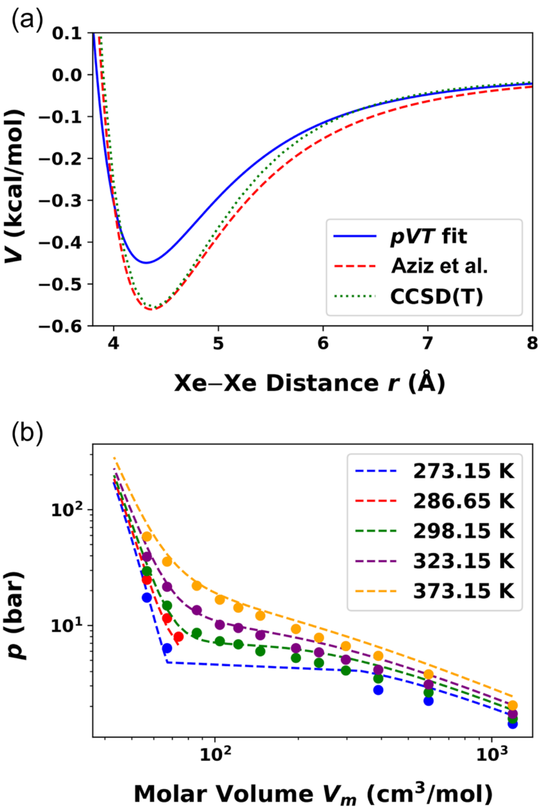

FIG. 1. (a) Two-body interaction potential V between Xe atoms computed by the Lennard-Jones potential function with the optimized LJ parameters (blue solid line) and from Aziz and Slaman (red dashed line).[54] The green dotted line shows the *ab initio* reference potential for a Xe–Xe atom pair at the CCSD(T)/cc-pV6Z level of theory corrected by higher coupled-cluster level contributions.[55] (b) Experimentally observed isotherms in the pVT diagram for pure xenon (dashed lines)[28] and computed pVT state points (full circles) with the optimized LJ parameters.

Figure 1(b) shows the comparison of the Xe–Xe interaction based on a LJ potential using the optimized LJ parameters and those from Aziz *et al.* The dissociation energies are 0.450 and 0.561 kcal/mol, respectively, at equilibrium separations of $r_e = 4.31$ and 4.36 Å. This compares with a dissociation energy of 0.556 kcal/mol and $r_e = 4.40$ Å from high-level CCSD(T)/cc-pV6Z calculations.[55] The zero point vibrational energy for a xenon pair is found to be 10.4 cm^{-1} (0.030 kcal/mol) experimentally[56] and 0.029 kcal/mol computationally using the CCSD(T)/cc-pV6Z potential data and a one-dimensional DVR method.[55]

Following previous work,[21] the local solvent reorganization lifetime τ_ρ was used to probe for distinct SCF properties and as a proxy to determine the computationally predicted critical density at the given temperature, following established routes.[57,58] Figures 2(a) and 2(b) show the computed τ_ρ for liquid xenon and SF$_6$, respectively. For the analysis, the cutoff radii for the first and second solvation shells of a local solvent residue cluster were estimated from the local minima of the respective radial distribution function $g(r)$ determined from the same trajectory. For both solvents, the maxima of τ_ρ for the simulated solvent concentration are close to the experimentally observed critical concentrations at the critical temperature. As was found in previous work,[57,58] the solvent fluctuation lifetime, τ_ρ, in LJ gas systems is a maximum for supercritical fluids at the critical concentration. This indicates that the supercritical dynamical properties are well captured by the solvent potential model and are one more manifestation of critical slowing, at least in pure xenon and SF$_6$.

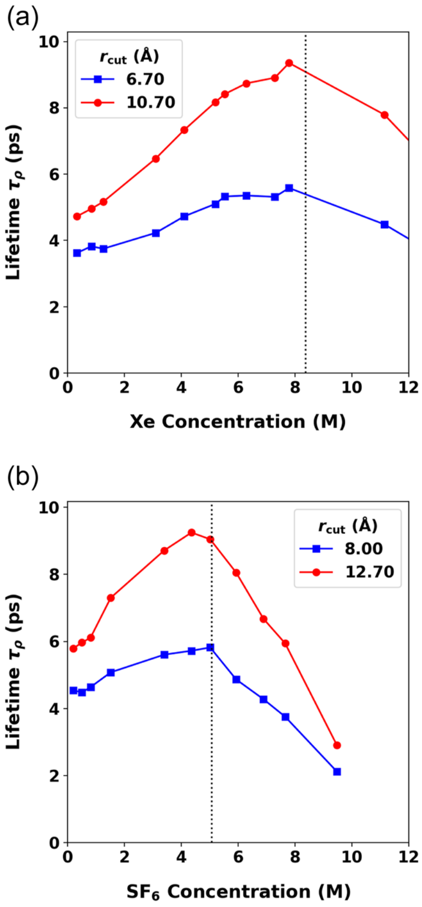

FIG. 2. Local solvent reorganization lifetime τ_ρ from the MD simulations of pure (a) xenon at $T = 291.2$ K and (b) SF$_6$ system at $T = 321.9$ K. The cutoff radii of the local solvent clusters are determined from the local minima in the respective radial distribution functions. The vertical dotted line marks the experimentally determined critical concentration at the critical temperatures of $c(\mathrm{Xe}) = 8.45$M and $c(\mathrm{SF_6}) = 5.02$M, respectively.[27]

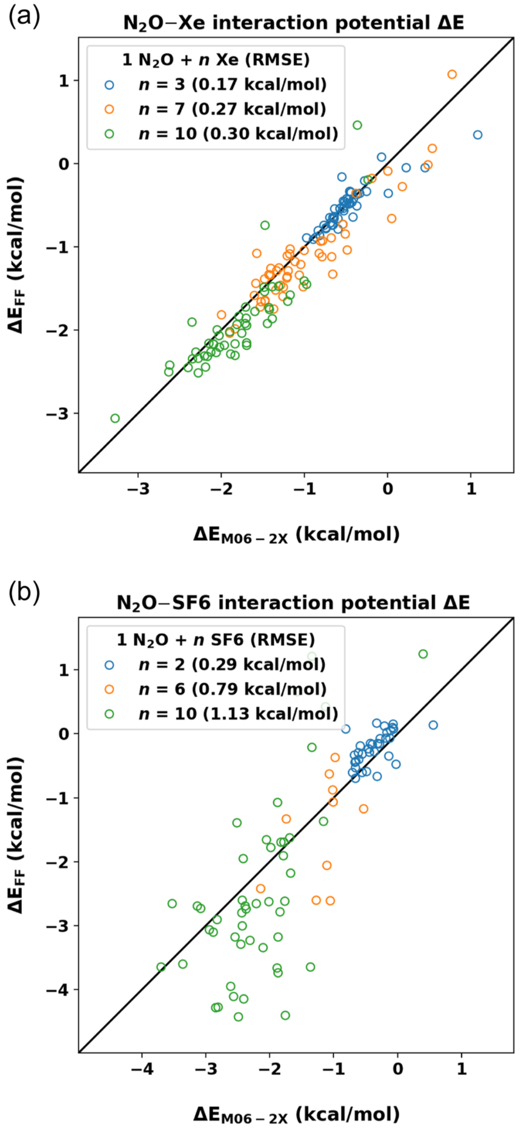

FIG. 3. Correlation plot of the optimized interaction potential model against the *ab initio* reference interaction energies between N$_2$O within (a) xenon and (b) SF$_6$ solvent clusters of different densities. The number of solvent particles in the cluster is given in the respective legend.

Intermolecular interactions

The intermolecular interactions between the N_2O solute and the Xe or SF_6 solvent were fit to reproduce counterpoise corrected *ab initio* reference interaction energies for various solute–solvent clusters. Figures 3(a) and 3(b) show the correlation between the modeled and reference interactions for the optimized LJ parameter of the N_2O atoms. The solute–solvent clusters with N_2O at their center have a maximum radius of 6.5 Å for Xe and 7.5 Å for SF_6. The number of solvent atoms or molecules within the cluster is representative of the local density of gaseous, supercritical, and liquid solvent environments, and the selection of cluster conformations is described in the Methods section.

The N_2O–Xe interaction in Fig. 3(a) with the optimized LJ parameter for N_2O reproduces the reference interaction energies with RMSEs from gaseous to liquid-like solvent clusters with 0.17, 0.27, and 0.30 kcal/mol. In contrast, for the N_2O–SF_6 interactions [see Fig. 3(b)], the RMSEs increase to 0.29, 0.79, and 1.13 kcal/mol. The interactions in supercritical and liquid-like cluster environments with $n = 6$ and 10 SF_6 molecules are overestimated due to stronger electrostatic interactions compared with Xe.

Rotational energy relaxation (RER)

From the simulations, the N_2O atom positions and velocities were recorded every 50 fs from the aggregate of 50 ns (5 × 10 ns) for each system and composition. The RER rates $1/\tau_{\mathrm{rot}}$ were then determined from the $E_{\mathrm{rot}}(t)$ autocorrelation function by fitting to a single–exponential function [see Eq. (4)], yielding a single RER time τ_{rot}. Figure 4 shows the RER rates in xenon and SF_6 retrieved from the corresponding calculated rotational energy correlation functions; see Figs. S1 and S2.

As an extension, a bi-exponential function was used to fit the rotational energy correlation functions. This yields two time scales: fast and slow RER times, $\tau_{\mathrm{rot,fast}}$ and $\tau_{\mathrm{rot,slow}}$, respectively, shown in Figure S3. In general, τ_{rot} from the single-exponential fit matches the slow component of the RER time $\tau_{\mathrm{rot,slow}}$ from which the respective rates are closest to the experimental results. Thus, only the fitting parameters of the single-exponential function will be discussed.

Analysis of the 2D IR experiments provided RER rates for N_2O molecules in gaseous, supercritical, and liquid solvent regions.[18–20] For xenon, a characteristic increase in $1/\tau_{\mathrm{rot}}$ for $c[\mathrm{Xe}] > 4\mathrm{M}$ was found, whereas for SF_6, critical slowing for $c[SF_6] > 4\mathrm{M}$ was observed [red traces in Figs. 4(a) and 4(b)]. Both measurements deviate from the results predicted by the simplest IBC model, which predicts a linear dependence between $c[\mathrm{solvent}]$ and $1/\tau_{\mathrm{rot}}$. From the simulations in xenon, however, the results follow that expected from IBC [blue symbols in Fig. 4(a)], whereas for SF_6, the computed results deviate around the predictions from IBC; see Fig. 4(b).

The agreement between the computed RER rates and the IBC model rather than the experimentally observed RER rates at supercritical solvent concentrations becomes apparent when scaling the rates with the concentration to yield the RER rates k_{rot}. From the slopes of the RER rate dependence of the IBC region in Fig. 4, the simulated N_2O RER rates are $k_{\mathrm{rot}}^{\mathrm{Xe}} = (3.67 \pm 0.25) \times 10^{10}\ \mathrm{s}^{-1}\ \mathrm{M}^{-1}$ and $k_{\mathrm{rot}}^{SF_6} = (1.25 \pm 0.12) \times 10^{11}\ \mathrm{s}^{-1}\ \mathrm{M}^{-1}$ for N_2O in Xe and SF_6, respectively. The 2DIR derived measured RER rates for N_2O in gaseous xenon and SF_6 solvent within the IBC region are $5.36 \times 10^{10}\ \mathrm{s}^{-1}\ \mathrm{M}^{-1}$ and $1.02 \times 10^{11}\ \mathrm{s}^{-1}\ \mathrm{M}^{-1}$, respectively, which are rather close to the simulation results.[20] The ratio $k_{\mathrm{rot}}^{SF_6}/k_{\mathrm{rot}}^{\mathrm{Xe}} \sim 3$ also qualitatively agrees with a factor of ~2 from the experiments.

Up to this point, the rotational energy was used to determine the correlation function and to obtain RER rates. To probe whether other angular-momentum-dependent quantities lead to similar conclusions, correlation functions for N_2O angular momentum $\vec{L}(t)$ and the squared angular momentum $|L(t)|^2$ were considered; see Figs. S4 and S5. Using $\vec{L}(t)$ yields higher rates than those from the squared angular momentum $|L(t)|^2$, which in turn closely matches the rates based on the rotational energy correlation function. This is not unexpected as the rotational energy is proportional to the squared angular momentum: $E_{\mathrm{rot}}(t) = |L(t)|^2/(2I)$ with I being the N_2O moment of inertia. The rates from $\vec{L}(t)$ are higher as they also include the reorientation of the rotational axis of N_2O known as rotational Brownian motion.[59]

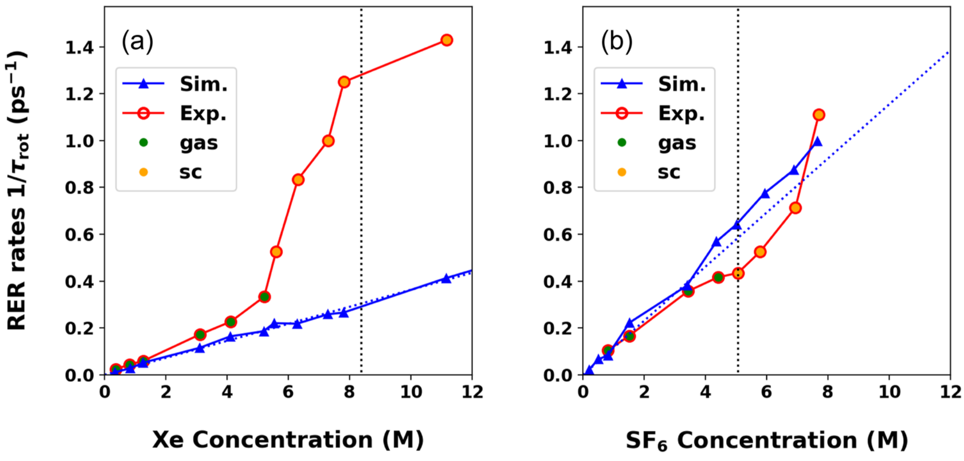

FIG. 4. RER rates from the RER times τ_{rot} of a fitted single-exponential function to the correlation function of the rotational energy $E_{\mathrm{rot}}(t)$ of N_2O in (a) xenon and (b) SF_6 at different solvent concentrations (blue solid lines). The red solid line with colored circle markers shows the experimentally measured RER rates and indicate the solvent state gaseous or supercritical (sc).[20] The blue dotted line is a linear extrapolation of the first three simulated RER rates. The vertical dotted lines mark the experimentally observed solvent concentration at the respective critical density of xenon and SF_6.

The respective correlation functions for $\vec{L}(t)$ and $|L(t)|^2$ of N_2O in xenon and SF_6 are shown in Figs. S6–S9. The correlation functions are the average of the correlation functions computed from each single sample run at the respective solvent concentration. The RER rates from fits to the correlation functions of the angular momentum $\vec{L}(t)$, squared angular momentum $|\vec{L}(t)|^2$, and rotational energy E_{rot} are shown in Figs. S10 and S11.

To conclude, for low solvent densities ($c[\mathrm{Xe}] < 4\mathrm{M}$ and $c[\mathrm{SF}_6] < 4\mathrm{M}$), the computed RER rates agree very favorably with experiments, whereas for higher densities, the deviations from the IBC model observed in the experiments are not correctly captured, specifically for xenon. Rather, the simulations follow the predicted behavior from the IBC model. As the deviations are systematic with increasing solvent concentration, it is conjectured that as the solvent concentration increases, the property probed by the experiment is not only the solute rotational energy. This is discussed further below. In addition, many-body effects may be insufficiently accounted for in the computational model, thus contributing to the lack of quantitative agreement particularly for N_2O in xenon at higher densities.

Collision analysis

The computed RER of N_2O in Xe and SF_6 followed the simple IBC model and is in disagreement with the experimentally observed rapid increase around $c[\mathrm{Xe}] > 5\mathrm{M}$ and critical slowing at the critical density for SF_6. To gain deeper insights into the solute–solvent interactions, the change in kinetic energy before and after N_2O–solvent collisions was further analyzed and decomposed into translational, rotational, and vibrational contributions of N_2O at different solvent densities.

Figure 5 shows the average absolute change in the kinetic energies of N_2O, xenon atoms, and SF_6 molecules upon collision. A collision between N_2O and solvent was considered to have occurred when any of the N_2O–Xe or N_2O–SF_6 atom separations is smaller than the sum of their atomic van der Waals radii (1.55, 1.52, 2.16, 1.80, 1.47 Å for N, O, Xe, S, and F, respectively).[60] The initial and final kinetic energies of N_2O and solvent were extracted from the simulation at the frame after crossing this van der Waals radii threshold from which the changes $|\Delta\bar{T}_\alpha|$ for α = total, vib, rot, trans and the corresponding distributions $P(|\Delta\bar{T}_\alpha|)$ were determined. Due to intramolecular energy flow and intermolecular exchange of kinetic energy between the solute and the surrounding solvent molecules during the contact time, the sum of changes in the kinetic energy contributions does not necessarily add up to the total kinetic energy difference.

Related to RER are changes in the N_2O rotational kinetic energy, $|\Delta\bar{T}_{\mathrm{rot}}|$; see Figs. 5(a) and 5(c) (red dotted line). For N_2O in Xe, $|\Delta\bar{T}_{\mathrm{rot}}|$ is lower than in SF_6 and the computed ratio $|\Delta\bar{T}^{\mathrm{SF}_6}_{\mathrm{rot}}/\Delta\bar{T}^{\mathrm{Xe}}_{\mathrm{rot}}| \sim 1.2$ compares with 1.9 from the experiments.[20] This indicates that in simulations with SF_6 as the solvent, the change in the N_2O rotational energy occurs not only due to collisions as for xenon. Rather, RER is also influenced by the longer-ranging, anisotropic intermolecular interactions between N_2O and the non-vanishing higher-order multipoles of SF_6. As the average change in vibrational kinetic energy in $|\Delta\bar{T}_{\mathrm{vib}}|$ (dotted-dashed green line) of N_2O is larger in SF_6 than in xenon, the overall change in the total kinetic energy $|\Delta\bar{T}_{\mathrm{tot}}|$ (black solid line) is considerably larger, whereas the changes in the translational kinetic energy $|\Delta\bar{T}_{\mathrm{trans}}|$ (blue

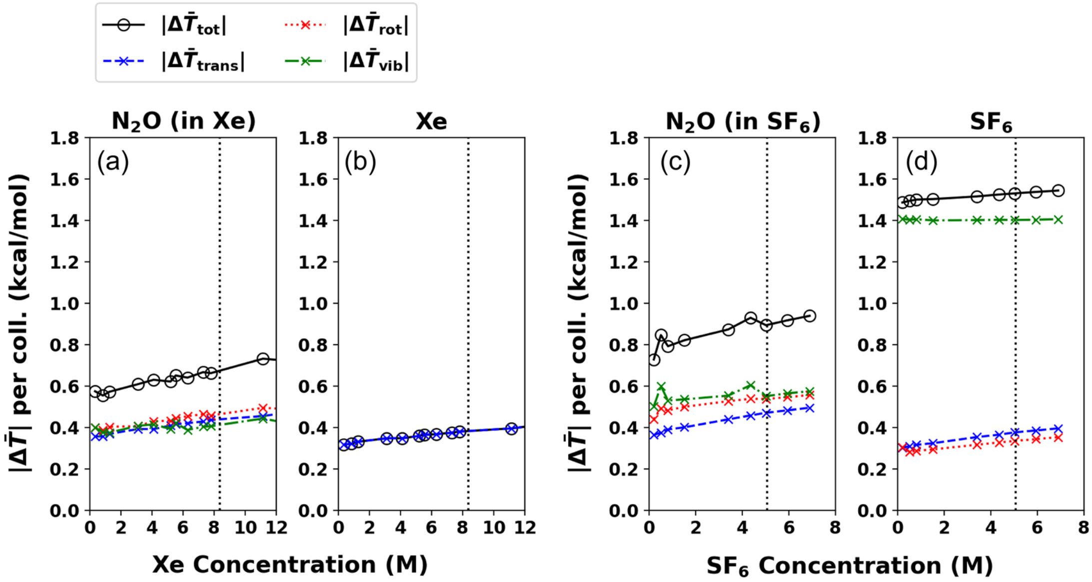

FIG. 5. Averaged absolute energy difference $|\Delta\bar{T}|$ of the total, translational, rotational, and vibrational kinetic energies after a collision between (a) and (b) N_2O and xenon and (c) and (d) N_2O and SF_6, respectively, at different solvent concentrations. The vertical dotted lines mark the experimentally observed solvent concentration at the respective critical density. Note the different system temperatures of 291.2 and 321.9 K for N_2O in xenon and SF_6, respectively.

dashed line) for the two solvents are comparable because the masses of xenon (131.3 u) and SF_6 (146.1 u) are similar.

The change in the kinetic energy contributions of the solvent particles, xenon and SF_6, after a collision with N_2O is shown in Figs. 5(b) and 5(d), respectively. At an atomistic level, the kinetic energy of a single xenon atom only consists of the translational contribution. Again, the translational contributions for xenon and SF_6 are comparable [blue symbols in Figs. 5(b) and 5(d)] due to their similar masses. However, because SF_6 has internal degrees of freedom, additional rotational and vibrational kinetic energy contributions arise and the total $|\Delta\bar{T}_{\text{tot}}|$ (open circles) for collisions with SF_6 are considerably larger than those of xenon. For SF_6, the rotational and translational contributions are similar in magnitude $|\Delta\bar{T}_{\text{rot}}| \sim |\Delta\bar{T}_{\text{trans}}|$, whereas $|\Delta\bar{T}_{\text{vib}}|$ is significantly larger. This is due to the larger number of vibrational degrees of freedom (15) compared with rotation (3) and translation (3). It is also interesting to note that the translational and rotational contributions for SF_6 depend on solvent-concentration, whereas the vibrational contribution does not. This is consistent with the analysis of the experimental data, which indicates that vibrational relaxation through intramolecular energy relaxation upon collision is IBC-like as opposed to rotational relaxation.[20]

Based on the RER rates $1/\tau_{\text{rot}}$, see Fig. 4, and the average collision frequency $\nu_{\text{coll}} = N_{\text{coll}}/t_{\text{sim}}$ ($t_{\text{sim}} = 50$ ns), it is also possible to compute the average number of collisions $Z_{\text{rot}} = \tau_{\text{rot}} \cdot \nu_{\text{coll}}$ required to rotationally relax the solute (N_2O). Here, N_{coll} is the number of collisions between N_2O and either xenon or SF_6, and $1/\tau_{\text{rot}}$ was already obtained from fitting a single-exponential decay to the rotational energy correlation function of N_2O in both solvents. Figures 6(a) and 6(b) show the computed average collision rate ν_{coll} and number of collisions Z_{rot} for the RER of N_2O in xenon and SF_6, respectively. The collision rate of N_2O with SF_6 [purple line in Fig. 6(a)] is higher than with xenon (magenta line) because of the higher simulation temperature (321.9 vs 291.2 K), the larger molecular volume occupied by SF_6 compared to a single xenon atom (based on atomic van der Waals radii), and the anisotropic electrostatic intermolecular interactions between N_2O and SF_6.

The experimentally reported $Z_{\text{rot}}^{\text{expt}}$ are 2.4 and 1.7 for the RER of N_2O in xenon and SF_6, respectively, based on a hard sphere model for both types of solvent molecules.[20,61] Within the IBC regime ($c[\text{Xe}] < 4\text{M}$ and $c[SF_6] < 4\text{M}$), $Z_{\text{rot}}^{\text{expt}}$ are larger than those from simulations. This is mostly due to the higher computed collision rate ν_{coll}, estimated from the inverse of the mean free collision time. Meanwhile, the ratio $Z_{\text{rot}}^{\text{expt, Xe}}/Z_{\text{rot}}^{\text{expt,}SF_6}$ is comparable but somewhat smaller (~1.4) than that from the simulations (~1.7). This is also related to lower simulated RER rates for N_2O in xenon within the IBC region compared with experiments for which the simulated RER rates for N_2O in SF_6 match well. Thus, the simulations reasonably agree well with the experiments for the RER of N_2O over solvent concentrations within the IBC regime. However, the simulations do not reproduce the steep increase or critical slowing in the RER rates in xenon and SF_6, respectively (see Fig. 4).

Vibrational energy relaxation

The VER lifetimes and rates were determined from the Landau–Teller formalism described in the Methods section. VER of a particular N_2O mode can involve either pure intramolecular relaxation or a combination of inter- and intramolecular processes, of which both can be obtained from MD simulations.[41–44,47] For this, the forces acting on the solute atoms derived only from the non-bonding solute–solvent interaction potential were extracted and projected along the normal mode vector of the asymmetric stretch vibration ν_{as} of N_2O; see Eq. (9).

For N_2O in SF_6 and from the experimental analysis,[20] the most effective vibrational relaxation channel of $\nu_{\text{as}}^{N_2O} \sim 2220$ cm^{-1} occurs through coupling with the symmetric N_2O stretch vibration

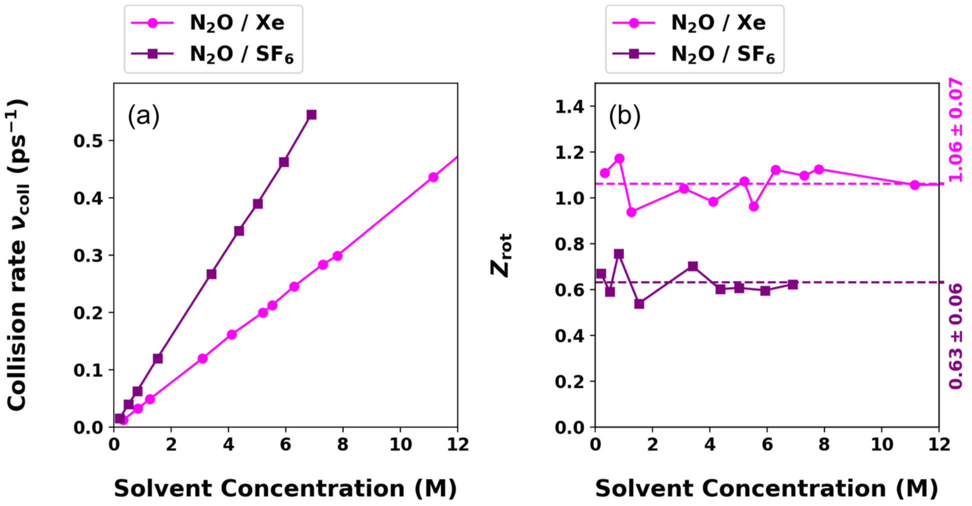

FIG. 6. (a) Average collision rates ν_{coll} between N_2O and xenon (magenta) and SF_6 (purple) according to the collision conditions using atom distances and van der Waals radii thresholds defined for this work. (b) Average number of collisions Z_{rot} for rotational relaxation of N_2O in xenon and SF_6 in the average and standard deviation displayed on the right axis.

$\nu_s^{N_2O} \sim 1280$ cm^{-1} and the threefold degenerate S–F stretch vibration $\nu_3^{SF_6} \sim 948$ cm^{-1}. Following the procedure outlined in the Methods section, the VER rates for $(\nu_s, \nu_{as}) = (0, 1) \rightarrow (1, 0)$ were computed. The forces of N_2O are projected along the normal mode vectors of ν_{as} obtained from instantaneous normal mode analysis at the respective frames, which can be interpreted as solvent friction. The Fourier transform of the correlation function of this quantity yields the frequency dependent friction function; see Figs. S16 and S17.

The VER lifetimes τ_{vib} for the relaxation $(0, 1) \rightarrow (1, 0)$ in N_2O were determined by the average of the friction function weighted by the frequency difference distribution $P(\nu_{as} - \nu_s)$. The resulting rates $1/\tau_{vib}$ from simulation and experiments[20] are shown in Fig. 7. The average frequency difference in the simulation was determined to be $\Delta\nu_{model} = 886$ cm^{-1} but $\Delta\nu_{exp} = 940$ cm^{-1} in experiments.[20] For consistency, the same distribution width centered around the experimentally observed frequency difference $\Delta\nu_{exp}$ was used to compute τ_{vib} [see the green dashed line in Fig. 7(b)]. Under the given conditions, the quantum correction factor increases the VER lifetimes τ_{vib} by about 4% [$Q(T_{Xe}, \Delta\nu_{model}) = 1.040$, $Q(T_{SF_6}, \Delta\nu_{model}) = 1.034$ or $Q(T_{SF_6}, \Delta\nu_{exp}) = 1.038$].

For N_2O in xenon, the computed N_2O VER rates for ν_{as} in Fig. 7(a) are on the ns^{-1} time scale for supercritical xenon and indicate a rather slow VER relaxation process, as expected. The average solvent concentration-weighted VER rate is $k_{VER} = 1/(\tau_{vib} \cdot c[Xe]) = (4.89 \pm 0.22) \times 10^8$ s^{-1} M^{-1}. Experimentally, $k_{VER}^{exp} \approx 5.1 \times 10^7$ s^{-1} M^{-1} ($\approx 8.5 \times 10^{-14}$ cm^3 s^{-1}), which corresponds to $\tau_{vib} \approx 2.5$ ns, was indirectly obtained at one solvent concentration ($[c(Xe)] = 7.8$M) from a small ($\sim 5\%$) reduction in the pump–probe decay signal within 200 ps.[20] At this concentration ($[c(Xe)] = 7.8$M), the computed rate $k_{VER}^{sim} = 5.00 \times 10^8$ s^{-1} M^{-1} is ~10 times faster compared with the estimate from the experiments. It should be noted that the Landau–Teller model was successfully applied to rather long VER times (~600 ps) for the case of CO in myoglobin.[44] Hence, it is likely that the Landau–Teller approach for VER is valid, but the limitations for N_2O in xenon arise due to the neglect of many-body interactions, in particular at high solvent densities.

Meanwhile, for N_2O in SF_6 [panel (b)], the computed VER rates obtained with the model frequency difference distribution around $\Delta\nu_{model}$ (blue line) are on the ps^{-1} time scale for gaseous and supercritical SF_6. Assuming a frequency difference distribution around the experimental value $\Delta\nu_{exp}$, the VER rates are higher by a factor of 2 (green dashed line). The VER of $\nu_{as}^{N_2O}$ is faster in SF_6 than in xenon due to the coupling with three-times degenerated S–F stretch

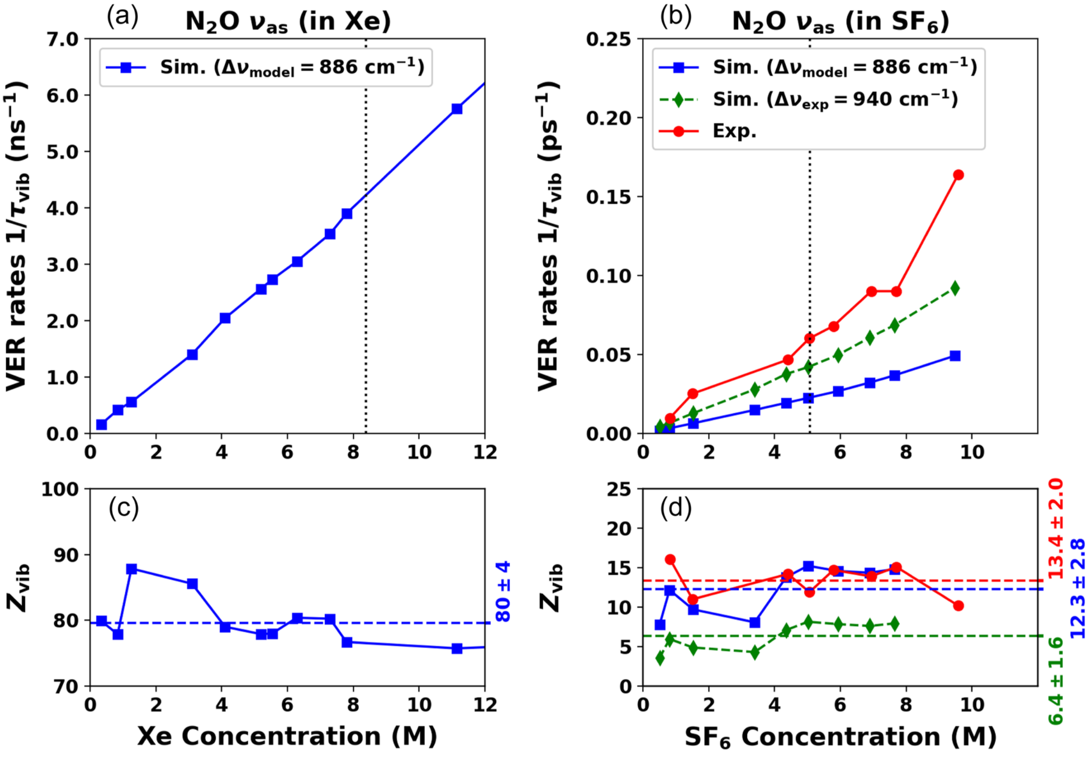

FIG. 7. Computed VER rates (blue squares) for $(\nu_s, \nu_{as}) = (0, 1) \rightarrow (1, 0)$ with frequency difference $\Delta\nu = \nu_{as} - \nu s$ computed from the frequency dependent friction function of the asymmetric stretch vibration of N_2O in (a) xenon and (b) SF_6 solvent at different solvent densities.[41,42] The frequency difference $\Delta\nu$ is given in the legend in brackets. For N_2O in SF_6 (b), experimental values are available from Ref. 20 and the VER rates are shown in assumption that $\Delta\nu$ matches the experimentally observed transition frequency of N_2O in SF_6 (green diamonds). Note the different unit representation of the VER rates in panels (a) and (b). The vertical dotted lines mark the experimentally observed solvent concentration at the respective critical density of xenon and SF_6, respectively. (c) and (d) Computed (and experimentally observed) number of collisions Z_{vib} for the vibrational relaxation of N_2O with average and standard deviation displayed on the right axis.

modes at $\nu_3 = 948\ \text{cm}^{-1}$, which is well visible by a peak around this wavenumber in the friction function in Fig. S17.

The available experimental data of the VER rates for N_2O ν_{as} in SF_6 [red circles in Fig. 7(b)] are still about four or two times faster than the VER rates computed with the frequency difference distribution from the model simulation or experimental observations, respectively. The computed VER rates, however, feature a linear increase with increasing SF_6 concentration, which corresponds to the VER rates of $k_{\text{VER}}(\Delta\nu_{\text{model}}) = (4.46 \pm 0.36) \times 10^9\ \text{s}^{-1}\ \text{M}^{-1}$ and $k_{\text{VER}}(\Delta\nu_{\text{exp}}) = (8.62 \pm 0.44) \times 10^9\ \text{s}^{-1}\ \text{M}^{-1}$. The experimentally reported VER rate for N_2O ν_{as} in gaseous SF_6 or the IBC regime is $k_{\text{VER,IBC}} = 1.56 \times 10^{10}\ \text{s}^{-1}\ \text{M}^{-1}$ $(2.6 \times 10^{-11}\ \text{cm}^3\ \text{s}^{-1})$.[20]

Scaling the computed VER lifetimes τ_{vib} with the estimated collision rate τ_{coll} reveals that for N_2O in xenon, an average of $Z_{\text{vib}} = \tau_{\text{vib}} \cdot \tau_{\text{coll}} = 80 \pm 4$ collisions between N_2O and xenon atoms is required to relax the asymmetric stretch vibration in N_2O. Using the experimentally estimated τ_{vib} would yield a yet larger value for Z_{vib} by one order of magnitude. For N_2O in SF_6, $Z_{\text{vib}}(SF_6) = 12.3 \pm 2.8$ or 6.4 ± 1.6 is about one order of magnitude smaller depending on whether $\Delta\nu_{\text{model}}$ or $\Delta\nu_{\text{exp}}$ is used for estimating the VER lifetime, respectively. From experiments, $Z_{\text{vib}}^{\text{expt.}} = 13.4 \pm 2.0$ collisions between N_2O and SF_6 are required. Due to differences in the estimated collision rate, $Z_{\text{vib}}^{\text{expt.}}$ is closer to the computed value from the VER rate estimation at $\Delta\nu_{\text{model}}$, which deviates more strongly from the experimental VER rates than the estimation at $\Delta\nu_{\text{exp}}$. The collision rate from the estimated mean free collision time—which is larger than the one obtained from counting collision events—together with the underestimated VER rate leads to closer agreement of computed and experimentally estimated Z_{vib} than the comparison of the VER.

If VER rates from simulations are computed using the experimentally reported frequency difference $\Delta\nu_{\text{exp}}$, the VER rates are ~0.8 times as fast compared with the experimentally measured VER rates for N_2O in SF_6. The first-order Landau–Teller model to compute the VER lifetimes used here only includes the term describing solvent friction, i.e., the influence of the solute–solvent interaction potential V_{int} on the normal mode $\nu_{\text{as}}^{N_2O}$. Shorter lifetimes might be obtained by including higher-order correction terms such as solvent-induced coupling to the solute–solvent interaction potential expression in Eq. (9). Such terms include the second derivative of V_{int} along the solute normal mode of $\nu_{\text{as}}^{N_2O}$ and $\nu_{\text{s}}^{N_2O}$ describing the relaxation pathway of intramolecular VER assisted by the solvent.[43]

DISCUSSION AND CONCLUSIONS

The present work provides an atom-resolved picture of rotational and vibrational energy relaxation of N_2O in xenon and SF_6 covering a wide range of thermodynamic states ranging from the gas phase to the liquid. In an effort to improve the solvent–solute interactions, the electrostatic and other nonbonded interactions were fit to reference electronic structure calculations at different levels of theory. While for VER satisfactory results compared with experiment were found, RER agrees with experiment only up to $c[\text{solvent}] \sim 4\text{M}$. For higher concentrations, the simulation follows the IBC model, whereas experimentally different behaviors are found for xenon and SF_6.

For N_2O in xenon, the experiments find a pronounced increase in the RER time as the concentration increases from 6 to 8M; see Fig. S4. The experiments are expected to report on the solvent rotational energy normalized autocorrelation function $\langle E_{\text{rot}}(0)E_{\text{rot}}(t)\rangle$. For low-density solvents, the experimental result could be reproduced almost quantitatively, whereas for increasing density, no discontinuous change in the RER time was found. Rather, the linear behavior—consistent with the IBC model—continued up to the highest simulated densities yield RER rates of $(3.67 \pm 0.25) \times 10^{10}\ \text{s}^{-1}\ \text{M}^{-1}$ and $(1.25 \pm 0.12) \times 10^{11}\ \text{s}^{-1}\ \text{M}^{-1}$ for N_2O in xenon and SF_6, respectively. These computed RER rates agree well with those from experiment within the IBC region of $5.36 \times 10^{10}\ \text{s}^{-1}\ \text{M}^{-1}$ and $1.02 \times 10^{11}\ \text{s}^{-1}\ \text{M}^{-1}$, respectively.

In search for a reason for the disagreement, additional correlation functions, including $\langle \vec{L}_{N_2O}(0)\vec{L}_{N_2O}(t)\rangle$, $\langle E_{\text{rot},N_2O}(0)E_{\text{rot},N_2O}(t)\rangle$, and $\langle \mu_{N_2O}(0)\mu_{N_2O}(t)\rangle$, were analyzed. However, all of them confirm the behavior of the computed $\langle \vec{L}^2_{N_2O}(0)\vec{L}^2_{N_2O}(t)\rangle$ correlation function. One possible explanation for the disagreement is the observation that with increasing density the solvent packing around the solute becomes so dense, that the properties of isolated N_2O (E_{rot,N_2O} or $\vec{L}_{N_2O}$) cannot be directly compared with the experimentally observed signals. In other words, analysis of the N_2O rotational motion without accounting for the coupling to the solvent shell(s)—as is usually done and was done here, too—becomes unrealistic. Rather, for sufficiently high solvent densities, the rotational motion of N_2O and the solvent molecules are coupled and the solvent molecules are "slaved" to the N_2O rotation. Quantum-mechanically, the rotational quantum number correlating with $\vec{L}_{N_2O}$ is a "good quantum number" for gas phase and low solvent densities, whereas this property is lost for increasing solvent density.

Analysis of the trajectories with regard to changes in kinetic energy (squared momentum transfer) between the collision partners (N_2O and xenon; N_2O and SF_6) revealed a larger average change for the rotational energy of N_2O when colliding with SF_6 than with xenon. The translational kinetic energy change of the solvent molecules xenon and SF_6 is comparable, whereas the additional rotational and vibrational degrees of freedom in SF_6 provide further energy transfer pathways compared with xenon.

Considering RER, the average number of collisions to rotationally relax N_2O over the concentration range considered are $Z_{\text{rot}}^{\text{Xe}} = 1.1$ and $Z_{\text{rot}}^{\text{SF6}} = 0.6$, respectively. This shows that RER for N_2O in SF_6 is about ~1.7 times more effective than in xenon, which is consistent with experiments. There, the values of 2.4 and 1.7 collisions are about 2–3 times larger for SF_6 compared with xenon, indicating a less efficient rotational relaxation per collision in the simulations. The largest deviations between experiments and the simulations are in the collision rates, which are twice as high when estimated from the inverse of the mean free collision times. Together with the simulated RER rates, this yields Z'_{rot} of 2.5 and 1.4 for N_2O in xenon and SF_6, respectively, which are much closer to the experiments. The relative change $|\Delta\bar{T}_{\text{rot}}^{SF_6}|/|\Delta\bar{T}_{\text{rot}}^{\text{Xe}}|$ is somewhat smaller but comparable to $|\Delta\bar{T}_{\text{vib}}^{SF_6}|/|\Delta\bar{T}_{\text{vib}}^{\text{Xe}}|$ depending on solvent concentration, which indicates that angular anisotropy of the intermolecular interactions influences RER.

The VER rates for the asymmetric N_2O stretch vibration ν_{as} in xenon were computed following the Landau–Teller approach and yielded $k_{\text{VER}} = (4.89 \pm 0.22) \times 10^8\ \text{s}^{-1}\ \text{M}^{-1}$, which is one order of magnitude faster compared with experiment. To put this comparison into context, it is useful to recall earlier experiments for O_2

vibrational relaxation in argon but at considerably lower temperatures.[46] The reported relaxation rates were five orders of magnitude smaller than experiments from entirely classical simulations, which changed to two orders smaller or one order larger than experiments depending on the quantum correction factor employed.[46] This work concluded that "relaxation rates on long time scales are extremely sensitive to details in the potential, and errors in the potential model could easily account for an order of magnitude discrepancy between theory and experiment." In SF_6, the computed rates are considerably faster (by one order of magnitude) with $(4.46 \pm 0.36) \times 10^9$ s^{-1} M^{-1} or $(8.62 \pm 0.44) \times 10^9$ s^{-1} M^{-1} depending on the applied frequency difference distribution $P(\nu_{as} - \nu_s)$ for the relaxation process $(\nu_s, \nu_{as}) = (0, 1) \rightarrow (1, 0)$. These rates are about ~0.4 to ~0.8 times the experimentally observed VER rate in the IBC regime at low solvent densities of 1.56×10^{10} s^{-1} M^{-1}, but also do the computed VER rates of N_2O ν_{as} in SF_6 around its critical density not show the effect of critical slowing as in the experiments [see Fig. 7(b)]. This deficiency of the simulation, however, is consistent with the missing effect of critical slowing in the computed RER rates for N_2O in SF_6.

In summary, this work presented a molecular-level study of rotational and vibrational energy relaxation of N_2O in xenon and SF_6 ranging from highly dilute to liquid phases of the solvent, including the supercritical regime. For regimes in which the IBC model is valid, almost quantitative agreement with experiment was found, whereas near the supercritical point, simulations and experimental findings disagree, in particular for RER. The most likely reason is that the effect of solvent packing is neglected if only the rotational motion of the solute (N_2O) is considered in the analysis—as is usually done—without accounting for solvent–solute coupling. The average number of collisions for rotational and vibrational relaxation from the simulations agrees rather well with those obtained from experiments. In conclusion, VER of N_2O across different solvent density regimes and RER in the low-density region can be characterized well at a molecular level, whereas for the higher-density regimes, analysis of the RER requires additional refinements.

SUPPLEMENTARY MATERIAL

The supplementary material includes system setups (Table S1), force field parameters (Table S2), various correlation functions (Figs. S1, S2, and S6–S9) with further evaluation results (Figs. S3–S5 and S10–S15), and the frequency-dependent friction functions (Figs. S16 and S17).

ACKNOWLEDGMENTS

This work was financially supported by the Swiss National Science Foundation (NCCR-MUST, Grant Nos. 200020_219779 and 200020-188724), the AFOSR, the University of Basel, and by the European Union's Horizon 2020 research and innovation program under the Marie Skłodowska-Curie Grant Agreement No. 801459-FP-RESOMUS. The authors acknowledge the support of the National Science Foundation, Grant No. CHE-2102427 (L.D.Z.), and the Boston University Photonics Center.

AUTHOR DECLARATIONS

Conflict of Interest

The authors have no conflicts to disclose.

Author Contributions

Kai Töpfer: Conceptualization (equal); Data curation (equal); Formal analysis (equal); Investigation (equal); Methodology (equal); Software (equal); Validation (equal); Visualization (equal); Writing – original draft (equal); Writing – review & editing (equal). **Shyamsunder Erramilli**: Conceptualization (equal); Data curation (equal); Formal analysis (equal); Investigation (equal); Supervision (equal); Writing – original draft (equal); Writing – review & editing (equal). **Lawrence D. Ziegler**: Conceptualization (equal); Data curation (equal); Formal analysis (equal); Funding acquisition (equal); Investigation (equal); Project administration (equal); Resources (equal); Supervision (equal); Validation (equal); Writing – original draft (equal); Writing – review & editing (equal). **Markus Meuwly**: Conceptualization (equal); Data curation (equal); Formal analysis (equal); Funding acquisition (equal); Investigation (equal); Methodology (equal); Project administration (equal); Resources (equal); Software (equal); Supervision (equal); Validation (equal); Writing – original draft (equal); Writing – review & editing (equal).

DATA AVAILABILITY

Relevant data for the present study are available at https://github.com/MMunibas/SCF_N2O/.

REFERENCES

[1] J. Foster and R. S. Miller, High pressure processes in chemical engineering, pp. 53–75.

[2] C. Guardiola, P. Olmeda, B. Pla, and P. Bares, "In-cylinder pressure based model for exhaust temperature estimation in internal combustion engines," Appl. Therm. Eng. **115**, 212–220 (2017).

[3] P. V. Farrell and B. D. Peters, "Droplet vaporization in supercritical pressure environments," Acta Astronaut. **13**, 673–680 (1986), Congress of the International Academy of Astronautics.

[4] O. Kajimoto, "Solvation in supercritical fluids: Its effects on energy transfer and chemical reactions," Chem. Rev. **99**, 355–390 (1999).

[5] Ž. Knez, E. Markočič, M. Leitgeb, M. Primožič, M. Knez Hrnčič, and M. Škerget, "Industrial applications of supercritical fluids: A review," Energy **77**, 235–243 (2014).

[6] G. Brunner, "Applications of supercritical fluids," Annu. Rev. Chem. Biomol. Eng. **1**, 321–342 (2010).

[7] M. K. Hrnčič, D. Cör, M. T. Verboten, and Ž. Knez, "Application of supercritical and subcritical fluids in food processing," Food Qual. Saf. **2**, 59–67 (2018).

[8] M. Perrut, "Supercritical fluid applications: Industrial developments and economic issues," Ind. Eng. Chem. Res. **39**, 4531–4535 (2000).

[9] P. B. Deshpande, G. A. Kumar, A. R. Kumar, G. V. Shavi, A. Karthik, M. S. Reddy, and N. Udupa, "Supercritical fluid technology: Concepts and pharmaceutical applications," PDA J. Pharm. Sci. Technol. **65**, 333–344 (2011).

[10] H. Machida, M. Takesue, and R. L. Smith, "Green chemical processes with supercritical fluids: Properties, materials, separations and energy," J. Supercrit. Fluids **60**, 2–15 (2011).

[11] S. C. Tucker, "Solvent density inhomogeneities in supercritical fluids," Chem. Rev. **99**, 391–418 (1999).

[12] K. Saitow, K. Otake, H. Nakayama, K. Ishii, and K. Nishikawa, "Local density enhancement in neat supercritical fluid due to attractive intermolecular interactions," Chem. Phys. Lett. **368**, 209–214 (2003).

[13] K. Nishikawa and T. Morita, "Inhomogeneity of molecular distribution in supercritical fluids," Chem. Phys. Lett. **316**, 238–242 (2000).

[14] K.-i. Saitow, H. Ochiai, T. Kato, and K. Nishikawa, "Correlation time of density fluctuation for supercritical ethylene studied by dynamic light scattering," J. Chem. Phys. **116**, 4985–4992 (2002).

[15] K.-i. Saitow, D. Kajiya, and K. Nishikawa, "Time evolution of density fluctuation in supercritical region. I. Non-hydrogen-bonded fluids studied by dynamic light scattering," J. Phys. Chem. A **109**, 83–91 (2005).

[16] G. Goodyear and S. C. Tucker, "Glass-like behavior in supercritical fluids: The effect of critical slowing down on solute dynamics," J. Chem. Phys. **111**, 9673–9677 (1999).

[17] G. Goodyear, M. W. Maddox, and S. C. Tucker, "The correlation between local and long-range structure in compressible supercritical fluids," J. Chem. Phys. **112**, 10327–10339 (2000).

[18] A. Mandal, G. Ng Pack, P. P. Shah, S. Erramilli, and L. D. Ziegler, "Ultrafast two-dimensional infrared spectroscopy of a quasifree rotor: *J* scrambling and perfectly anticorrelated cross peaks," Phys. Rev. Lett. **120**, 103401 (2018).

[19] G. Ng Pack, M. C. Rotondaro, P. P. Shah, A. Mandal, S. Erramilli, and L. D. Ziegler, "Two-dimensional infrared spectroscopy from the gas to liquid phase: Density dependent *J*-scrambling, vibrational relaxation, and the onset of liquid character," Phys. Chem. Chem. Phys. **21**, 21249–21261 (2019).

[20] M. C. Rotondaro, A. Jain, S. Erramilli, and L. D. Ziegler, "Ultrafast 2DIR comparison of rotational energy transfer, isolated binary collision breakdown, and near critical fluctuations in Xe and SF_6 solutions," J. Chem. Phys. **157**, 174305 (2022).

[21] K. Töpfer, D. Koner, S. Erramilli, L. D. Ziegler, and M. Meuwly, "Molecular-level understanding of the rovibrational spectra of N_2O in gaseous, supercritical, and liquid SF_6 and Xe," J. Chem. Phys. **158**, 144302 (2023).

[22] O. T. Unke and M. Meuwly, "Toolkit for the construction of reproducing kernel-based representations of data: Application to multidimensional potential energy surfaces," J. Chem. Inf. Model. **57**, 1923–1931 (2017).

[23] D. Koner, J. C. San Vicente Veliz, R. J. Bemish, and M. Meuwly, "Accurate reproducing kernel-based potential energy surfaces for the triplet ground states of N_2O and dynamics for the $N + NO \leftrightarrow O + N_2$ and $N_2 + O \rightarrow 2N + O$ reactions," Phys. Chem. Chem. Phys. **22**, 18488–18498 (2020).

[24] H.-J. Werner, P. J. Knowles, F. R. Manby, J. A. Black, K. Doll, A. Heßelmann, D. Kats, A. Köhn, T. Korona, D. A. Kreplin *et al.*, "The Molpro quantum chemistry package," J. Chem. Phys. **152**, 144107 (2020).

[25] D. Dellis and J. Samios, "Molecular force field investigation for sulfur hexafluoride: A computer simulation study," Fluid Phase Equilib. **291**, 81–89 (2010).

[26] R. M. Stephenson, S. Malanowski, and D. Ambrose, *Handbook of the Thermodynamics of Organic Compounds; Section on Vapor-Liquid Critical Constants of Fluids* (Elsevier, 1987).

[27] W. Haynes, *CRC Handbook of Chemistry and Physics* (CRC Press, 2014), pp. 6–85.

[28] A. Michels, T. Wassenaar, and P. Louwerse, "Isotherms of xenon at temperatures between 0°C and 150°C and at densities up to 515 Amagats (pressures up to 2800 atmospheres)," Physica **20**, 99–106 (1954).

[29] J. A. Nelder and R. A. Mead, "A simplex method for function minimization," Comput. J. **7**, 308–313 (1965).

[30] M. Devereux, S. Raghunathan, D. G. Fedorov, and M. Meuwly, "A novel, computationally efficient multipolar model employing distributed charges for molecular dynamics simulations," J. Chem. Theory Comput. **10**, 4229–4241 (2014).

[31] O. T. Unke, M. Devereux, and M. Meuwly, "Minimal distributed charges: Multipolar quality at the cost of point charge electrostatics," J. Chem. Phys. **147**, 161712 (2017).

[32] M. Devereux, M. Pezzella, S. Raghunathan, and M. Meuwly, "Polarizable multipolar molecular dynamics using distributed point charges," J. Chem. Theory Comput. **16**, 7267–7280 (2020).

[33] M. J. Frisch, G. W. Trucks, H. B. Schlegel, G. E. Scuseria, M. A. Robb, J. R. Cheeseman, G. Scalmani, V. Barone, G. A. Petersson, H. Nakatsuji *et al.*, *Gaussian 16, Revision C.01*, Gaussian, Inc, Wallingford, CT, 2016.

[34] T. N. Olney, N. Cann, G. Cooper, and C. Brion, "Absolute scale determination for photoabsorption spectra and the calculation of molecular properties using dipole sum-rules," Chem. Phys. **223**, 59–98 (1997).

[35] M. Gussoni, M. Rui, and G. Zerbi, "Electronic and relaxation contribution to linear molecular polarizability. An analysis of the experimental values," J. Mol. Struct. **447**, 163–215 (1998).

[36] M. A. Branch, T. F. Coleman, and Y. Li, "A subspace, interior, and conjugate gradient method for large-scale bound-constrained minimization problems," SIAM J. Sci. Comput. **21**, 1–23 (1999).

[37] S. Boys and F. Bernardi, "The calculation of small molecular interactions by the differences of separate total energies. Some procedures with reduced errors," Mol. Phys. **19**, 553–566 (1970).

[38] S. Grimme, J. Antony, S. Ehrlich, and H. Krieg, "A consistent and accurate *ab initio* parametrization of density functional dispersion correction (DFT-D) for the 94 elements H-Pu," J. Chem. Phys. **132**, 154104 (2011).

[39] B. R. Brooks, C. L. Brooks III, A. D. Mackerell, Jr., L. Nilsson, R. J. Petrella, B. Roux, Y. Won, G. Archontis, C. Bartels, S. Boresch *et al.*, "CHARMM: The biomolecular simulation program," J. Comput. Chem. **30**, 1545–1614 (2009).

[40] L. Martínez, R. Andrade, E. G. Birgin, and J. M. Martínez, "Packmol: A package for building initial configurations for molecular dynamics simulations," J. Comput. Chem. **30**, 2157–2164 (2009).

[41] R. M. Whitnell, K. R. Wilson, and J. T. Hynes, "Vibrational relaxation of a dipolar molecule in water," J. Chem. Phys. **96**, 5354–5369 (1992).

[42] R. Rey and J. T. Hynes, "Vibrational phase and energy relaxation of CN^- in water," J. Chem. Phys. **108**, 142–153 (1998).

[43] A. Morita and S. Kato, "Vibrational relaxation of azide ion in water: The role of intramolecular charge fluctuation and solvent-induced vibrational coupling," J. Chem. Phys. **109**, 5511–5523 (1998).

[44] D. E. Sagnella, J. E. Straub, T. A. Jackson, M. Lim, and P. A. Anfinrud, "Vibrational population relaxation of carbon monoxide in the heme pocket of photolyzed carbonmonoxy myoglobin: Comparison of time-resolved mid-IR absorbance experiments and molecular dynamics simulations," Proc. Natl. Acad. Sci. U. S. A. **96**, 14324–14329 (1999).

[45] S. A. Egorov and J. L. Skinner, "A theory of vibrational energy relaxation in liquids," J. Chem. Phys. **105**, 7047–7058 (1996).

[46] K. Everitt, S. Egorov, and J. Skinner, "Vibrational energy relaxation in liquid oxygen," Chem. Phys. **235**, 115–122 (1998).

[47] K. F. Everitt and J. L. Skinner, "Vibrational energy relaxation of oxygen in liquid mixtures with argon," J. Chem. Phys. **110**, 4467–4470 (1999).

[48] J. S. Bader and B. J. Berne, "Quantum and classical relaxation rates from classical simulations," J. Chem. Phys. **100**, 8359–8366 (1994).

[49] J. L. Skinner and K. Park, "Calculating vibrational energy relaxation rates from classical molecular dynamics simulations: Quantum correction factors for processes involving vibration−vibration energy transfer," J. Phys. Chem. B **105**, 6716–6721 (2001).

[50] J. Tennyson, M. A. Kostin, P. Barletta, G. J. Harris, O. L. Polyansky, J. Ramanlal, and N. F. Zobov, "DVR3D: A program suite for the calculation of rotation–vibration spectra of triatomic molecules," Comput. Phys. Commun. **163**, 85–116 (2004).

[51] G. Herzberg, *Infrared and Raman Spectra of Polyatomic Molecules* (D. Van Nostrand Company, Inc., New York, 1945).

[52] G. Herzberg and L. Herzberg, "Rotation-vibration spectra of diatomic and simple polyatomic molecules with long absorbing paths VI. The spectrum of nitrous oxide (N_2O) below 1.2μ," J. Chem. Phys. **18**, 1551–1561 (1950).

[53] R. H. Kagann, "Infrared absorption intensities for N_2O," J. Mol. Spectrosc. **95**, 297–305 (1982).

[54] R. A. Aziz and M. Slaman, "On the Xe-Xe potential energy curve and related properties," Mol. Phys. **57**, 825–840 (1986).

[55] R. Hellmann, B. Jäger, and E. Bich, "State-of-the-art *ab initio* potential energy curve for the xenon atom pair and related spectroscopic and thermophysical properties," J. Chem. Phys. **147**, 034304 (2017).

[56] D. E. Freeman, K. Yoshino, and Y. Tanaka, "Vacuum ultraviolet absorption spectrum of the van der Waals molecule Xe_2. I. Ground state vibrational structure, potential well depth, and shape," J. Chem. Phys. **61**, 4880–4889 (1974).

[57] M. W. Maddox, G. Goodyear, and S. C. Tucker, "Origins of atom-centered local density enhancements in compressible supercritical fluids," J. Phys. Chem. B **104**, 6248–6257 (2000).

[58] M. W. Maddox, G. Goodyear, and S. C. Tucker, "Effect of critical slowing down on local-density dynamics," J. Phys. Chem. B **104**, 6266–6270 (2000).

[59] B. J. Berne and R. Pecora, *Dynamic Light Scattering: With Applications to Chemistry, Biology, and Physics* (Courier Corporation, 2000).

[60] A. Bondi, "van der Waals volumes and radii," J. Phys. Chem. **68**, 441–451 (1964).

[61] J. Yardley, *Introduction to Molecular Energy Transfer* (Academic Press, New York, 1980).